

A robust shape model for blood vessels analysis

Pau Romero^a, Abel Pedrós^a, Rafael Sebastian^a, Miguel Lozano^a and Ignacio García-Fernández^{a,1}

^aCoMMLab – Computational Multiscale Simulation Lab. University of Valencia. Spain.

Abstract

The availability of digital twins for the cardiovascular system will enable insightful computational tools both for research and clinical practice. This, however, demands robust and well defined models and methods for the different steps involved in the process. We present a vessel coordinate system (VCS) that enables the unambiguous definition of locations in a vessel section, by adapting the idea of cylindrical coordinates to the vessel geometry. Using the VCS model, point correspondence can be defined among different samples of a cohort, allowing data transfer, quantitative comparison, shape coregistration or population analysis. Furthermore, the VCS model allows for the generation of specific meshes (e.g. cylindrical grids, o grids) necessary for an accurate reconstruction of the geometries used in fluid simulations. We provide the technical details for coordinates computation and discuss the assumptions taken to guarantee that they are well defined. The VCS model is tested in a series of applications. We present a robust, low dimensional, patient specific vascular model and use it to study phenotype variability analysis of the thoracic aorta within a cohort of patients. Point correspondence is exploited to build an haemodynamics atlas of the aorta for the same cohort. The atlas originates from fluid simulations (Navier-Stokes with Finite Volume Method) conducted using OpenFOAMv10. We finally present a relevant discussion on the VCS model, which covers its impact in important areas such as shape modeling and computer fluids dynamics (CFD).

Keywords: Blood vessel anatomy; Parametric vascular modeling; Coordinate system; CFD Simulations; Digital twin; Patient-specific modeling.

¹Corresponding Author <ignacio.garcia@uv.es>.

Tel. +34 96 354 3064. Fax. +34 96 354 47 68.

Article published in Applied Mathematics and Computation: <https://doi.org/10.1016/j.amc.2024.129078>

1 Introduction

Encoding and representation of anatomy is one of the grounding pieces for the development of the so-called digital twin (Corral-Acero et al., 2020). When building a digital patient, data from different sources has to be put together on a common anatomical substrate (Bayer et al., 2012; Gil et al., 2019; Lopez-Perez et al., 2019; Salmasi et al., 2021). The combination of mechanistic models with data science models has proven to be a powerful tandem for interpreting simulation results, generating data for model training, or synthesizing large virtual cohorts for in-silico trials (Alber et al., 2019; Baker et al., 2018; Geronzi et al., 2023; Lamata, 2018; Niederer et al., 2020; Romero et al., 2021; Thamsen et al., 2021). These computational tools require suitable representations of the anatomy to encode patient information, which means representations that are independent of the patient from a computational point of view (Schuler et al., 2021).

In the case of modeling vascular anatomy, we find different technical solutions and strategies that we can classify in four groups. Some authors use a set of anatomical traits that are relevant for their clinical problem. In order to study characteristics associated to ascending aorta aneurysm, Cosentino et al. (2020) define a reduced set of 15 anatomical features and relate them with biomechanical descriptors biomarkers. This approach is not intended, however, to provide an encoding of the anatomy beyond the goal of the study, and it does not allow, for instance, the reconstruction of an aorta from its characteristics. A common approach for a computational description of vessels is to extract their centerline and analyze the morphology of

cross sections. Following this approach, Antiga and Steinman (2004); Antiga et al. (2008) build models for bifurcating vessels by treating their lumen as the union of spheres located along the centerline. Medrano-Gracia et al. (2016) build an atlas of vessel bifurcations also by studying the centerline of a vessel tree and their cross sections at regular distances. In order to have an analytic description of the wall of a vessel, some authors sweep closed curves, such as ellipses (Alvarez et al., 2017) or polynomials (Urlick et al., 2019; Zhang et al., 2007), along the centerline. A more general approach, in the sense that it is not specific for vessels, is the use of *large deformation diffeomorphic metric mappings* (Durrleman et al., 2009) to encode the geometry. This technique characterizes geometries through the integral of vector fields on their surface, and has been successfully applied to study the variability of aortic arc shape (Bruse et al., 2017) but also to analyze other organs such as the whole heart (Rodero et al., 2021). When machine learning models are to be involved, it is often a requirement that all the samples use a common encoding; the same dimensionality, with common meaning for all features. With this aim, Liang and coauthors use a reference triangle mesh for the wall of the thoracic aorta and project its points onto the wall of each sample. By doing so, all the aortas are described by a template, adapted to the patient specific phenotype. The template is, then, fed into a neural network to estimate functional biomarkers of the aorta (Liang et al., 2017, 2018, 2020).

This diversity of methods enable descriptions tailored to the requirements of each problem. However, not all methods are equally adequate for inter-patient comparison or for population based statistical studies. Furthermore, this diversity of

approaches might hamper the reproducibility and the comparability of different research works. For these reasons, some authors are stressing the importance of having robust and standardized methods for all the phases of the development and analysis of multiscale biophysical models and simulation results (Bayer et al., 2018; Niederer et al., 2020; Roney et al., 2019; Schuler et al., 2021; Urick et al., 2019).

In this paper, we propose a new representation of the anatomy of blood vessels. We present a Vessel Coordinate System (VCS) that serves as a reference to describe a location on the vessel wall or in its lumen. The VCS enables the quantitative comparison of data fields defined on a set of vessels corresponding to the same anatomical section, and serves as a tool for the analysis and visualization of fields defined on a vessel. We provide a detailed description of the different steps to build the reference system, and justify the particular decisions, with the aim of reproducibility, anatomy comparability, and robustness. We show that, on the proposed VCS, a robust, low dimensional, differentiable representation of the vessel surface can be built, enabling point-wise comparison of anatomies and of data fields defined on them, without ambiguity and at a very reasonable computational cost. After defining the VCS in Section 2, we show some use cases. In Section 3.1 a patient specific vascular model for the thoracic aorta is built from medical image data. In Section 3.2 a statistical shape model of the aorta is developed from a cohort of patients, and, finally, in Section 3.3 an haemodynamic atlas is computed for that cohort.

2 Material and methods

We have developed a coordinate system that enables a unique description of a point inside the vessel lumen or on the vessel wall. Our scheme is similar to the one presented in (Bayer et al., 2018) to define a coordinate system on the ventricle.

2.1 Material

We have used a data set of 30 thoracic aortas, to test our methodology on a wide range of anatomies with variable ratios of curvature and diameter. The set of anatomies corresponds to a cohort of 30 patients with ages ranging from 78 to 89 years old, suffering from aortic valve stenosis. The cohort has variability of ascending aorta diameters, with values ranging from around 3.5cm to over 6cm in some patients with aneurysm. Expert radiologists manually segmented the aortas from computerized tomography images, acquired at the mesosystole phase of the cardiac cycle. Since the VCS is restricted to single branch vessels, the supra-aortic branches as well as the coronary arteries were removed in all the cases. The final input data set used in this study was the set of 30 anonymized triangular surface meshes (see Fig. 1). All the data acquisition process met the requirements of the Declaration of Helsinki and was approved by the institutional ethics committee.

2.2 Vessel coordinate system

The wall of a vessel section –with no bifurcations– can be considered as homeomorphic (i.e. can be transformed through a continuous bijection) to a cylinder. The proposed VCS is a generalization of the cylindrical coordinate system applied to the vessel, as in (Bersi et al., 2016, 2019; Meister et al., 2020; Rego

et al., 2021), where they align the longitudinal axis of the vessel with the z axis (corresponding to *height*) of the cylindrical reference system. However, for this alignment to be possible, a longitudinal axis must be defined, which limits the application of cylindrical coordinates to almost straight vessel sections.

A natural generalization to this scheme is to substitute the longitudinal axis by a regular parametric curve inside the vessel, and to define a local reference frame at every point of the curve. Then, a location $\mathbf{x} \in \mathbb{R}^3$ inside the vessel’s lumen can be identified by the longitudinal location of the closest point of the curve to \mathbf{x} and by the coordinates of \mathbf{x} in the local reference frame corresponding to that closest point. We describe how this coordinate system can be built so that both the curve and the local reference frames are properly defined in a wide range of situations.

2.2.1 Definition of the vessel coordinate system

We define the VCS for a vessel segment that is limited by two cross sections. We assume that the region of interest has already been segmented, and that we have identified the location of the wall, either as a triangle mesh or as a volumetric representation. We assume that the two ends of the vessel section are defined by two planes A and B approximately orthogonal to the vessel direction and that we have two points $\mathbf{p}_A \in A$ and $\mathbf{p}_B \in B$ inside the vessel lumen, as shown in Fig. 2.

For this segment, we start by building a regular parametric curve, $\mathbf{c} : I \rightarrow \mathbb{R}^3$, that defines the longitudinal direction of the vessel segment, and a local reference frame defined on the curve, $\{\mathbf{t}(t), \mathbf{v}_1(t), \mathbf{v}_2(t)\}$, with \mathbf{t} the unitary tangent to \mathbf{c} . Then, given a point $\mathbf{x} \in \mathbb{R}^3$ on the wall or inside the lumen of the vessel, we define its cylindrical coordinates as

$$\tau = \operatorname{argmin}_{t \in I} \{\|\mathbf{x} - \mathbf{c}(t)\|\}; \quad (1)$$

$$\theta = \operatorname{angle}_{\mathbf{t}}(\mathbf{v}_1(\tau), \mathbf{x} - \mathbf{c}(\tau)), \quad (2)$$

$$\rho = \|\mathbf{x} - \mathbf{c}(\tau)\|; \quad (3)$$

where the function $\operatorname{angle}_{\mathbf{t}}(\cdot, \cdot)$ gives the angle between two vectors, rotating around the direction defined by \mathbf{t} . The bottom diagram in Fig. 2 shows the coordinate system for a point inside the vessel. The parameter $\tau \in I$ represents the longitudinal position of \mathbf{x} in the vessel segment, while $\theta \in [0, 2\pi]$ and $\rho \in \mathbb{R}^+$ are the polar coordinates of \mathbf{x} in the reference frame $\{\mathbf{v}_1, \mathbf{v}_2\}$ defined at $\mathbf{c}(\tau)$. Given three values $\tau \in I$, $\theta \in [0, 2\pi]$ and $\rho \in \mathbb{R}^+$, they determine a point in \mathbb{R}^3 that meets the previous definition by means of

$$\mathbf{x}(\tau, \theta, \rho) = \mathbf{c}(\tau) + \rho(\mathbf{v}_1 \cos(\theta) + \mathbf{v}_2 \sin(\theta)). \quad (4)$$

For this coordinate system to be well defined, the longitudinal curve, \mathbf{c} , and the local reference frame, $\{\mathbf{v}_1(t), \mathbf{v}_2(t)\}$, have to be, in turn, properly defined. In this section we describe the basic properties each piece of the VCS needs to have, and we explain how to compute them meeting these requirements.

2.2.2 Computation of the longitudinal curve

The first step to compute the VCS is to compute the curve that determines the longitudinal direction of the vessel segment. We compute this curve as the centerline or medial axis of the geometry (Blum, 1967). In our work we build the centerline as the



Figure 1: Sagittal view of the 30 thoracic aorta meshes used for the study.

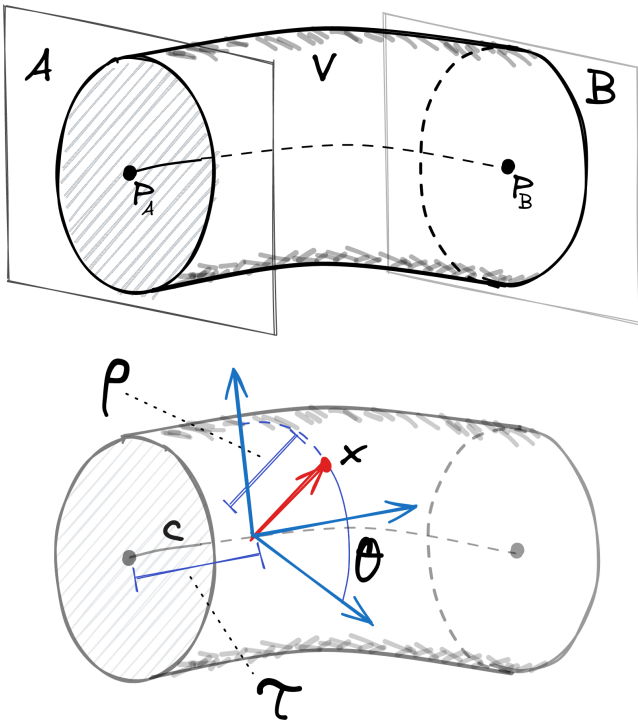


Figure 2: The Vessel Coordinate System is defined on a vessel section V , confined by two cross sections A , and B (top). The longitudinal axis of the cylinder is represented by a curve, c , on which a local reference frame is defined, $\{t(t), v_1(t), v_2(t)\}$ (bottom figure, arrows in blue), with t the unitary tangent to c . Given a point x , its coordinates are its longitudinal location along the curve, τ , and the polar coordinates of x in the plane orthogonal to the curve containing x , (ρ, θ) , represented in red in the figure.

curve c that connects the two planes A and B and that maximizes the minimum distance from the vessel wall to every point of c .

First, on a volumetric discretization of the vessel lumen, which can be obtained directly from medical image data or generated from the wall points, we compute the distance field with respect to the wall. Then, we build a discrete path that traverses the lumen points maximizing the distance to the wall along the curve. In order to do this, we use the A^* graph search algorithm, taking the inverse of the distance scalar field as the

cost function, and a neighborhood defined by distance (Romero et al., 2022). We finally build a differentiable curve by adjusting cubic B-spline to the set of points that form the discrete path. Without loss of generality, we will take a parametrization of the curve with constant velocity and $I = [0, 1]$.

2.2.3 Local reference frame

The definition of the angular coordinate, θ , requires a stable angular origin in the normal plane along the centerline. Moreover, if comparison between different patients' vessels is one of our goals, we need to provide stability also among the different anatomies of a cohort. A reference frame based on the intrinsic geometry of the curve, such as the Frenet frame, would not provide such stability and could lead to undetermined directions (e.g. where the curvature vanishes) (Piccinelli et al., 2009). Instead, we rely on the definition of an arbitrary reference frame at the beginning of the curve $c(0)$, together with its parallel transport along the curve. The parallel transport of a vector orthogonal to a curve sweeps the vector along the curve in a way that it changes the minimum required to keep it inside the normal plane (Guo et al., 2013). More formally, given a parametric curve $c : [0, 1] \rightarrow \mathbb{R}^3$, and a vector $v^0 \perp t(0)$, the vector field $v(s)$ is the parallel transport of v^0 if its derivative w.r.t. s can be entirely expressed in terms of the tangent vector, t , i.e. $\dot{v}(s) = g(s)t(s)$ for some function $g(s)$. The interested reader will find further detail in (Bishop, 1975; Carroll et al., 2013).

In order to build a stable reference frame along the centerline, we start by defining a reference frame at the initial point of the curve, $\{v_1^0, v_2^0\}$, and compute its parallel transport, $\{v_1(s), v_2(s)\}$, using a forward Euler integration scheme as follows. Assuming that the parallel transport has been computed up to $s \geq 0$, and given $h > 0$, we compute the frame at $s + h$ by rotating $v_1(s)$ and $v_2(s)$ by an angle $\alpha = \arccos(t(s) \cdot t(s + h))$ around the direction defined by $r = t(s) \times t(s + h)$. From now on, we will refer to the local reference frame at a point of the curve $c(s)$ as $\{v_1, v_2\}$, dropping the parameter s unless it leads to ambiguity.

2.2.4 Computation of the coordinates for a point

Next, we describe the procedure we use to compute the coordinates of a given point $x \in \mathbb{R}^3$. For now, we assume that

the point \mathbf{x} is such that the minimization problem defined by Eq. (1) has a unique solution. Later on, in Section 4, we will discuss why this is a reasonable assumption and how to overcome situations in which this assumption could fail to be true.

The first step is to define the reference frame for the initial point of the curve, $\{\mathbf{v}_1^0, \mathbf{v}_2^0\}$. The election of this reference frame is arbitrary and should be done taking in consideration the particular goals of the study, e.g., in all our tests, we take \mathbf{v}_1^0 so that the centroid (the average) of the points of the wall is contained in the plane defined by $\mathbf{t}(0)$ and, \mathbf{v}_1^0 .

Longitudinal coordinate, τ . In order to compute τ we need to solve Eq. (1), which stands for finding the closest point $\mathbf{c}(\tau)$ to \mathbf{x} on the curve \mathbf{c} . The optimality condition for that problem states that the tangent to the curve, \mathbf{t} , and the vector $\mathbf{c}(\tau) - \mathbf{x}$ must be orthogonal. Thus, we can directly minimize Eq. (1) or solve the nonlinear equation $\mathbf{t}(\tau) \cdot (\mathbf{c}(\tau) - \mathbf{x}) = 0$. In either case, we can benefit from the fact that \mathbf{c} is an order 3 polynomial for which we have its derivatives analytically.

Local polar coordinates, ρ, θ . Once τ has been computed for \mathbf{x} , the value of the radial coordinate, ρ , which stands for the distance from \mathbf{x} to the curve \mathbf{c} , is immediately obtained as $\rho = \|\mathbf{c}(\tau) - \mathbf{x}\|$. The computation of the angular coordinate, θ , requires the local reference frame $\{\mathbf{v}_1(\tau), \mathbf{v}_2(\tau)\}$. This reference frame is obtained, as described previously, by solving the parallel transport of the initial reference frame $\{\mathbf{v}_1^0, \mathbf{v}_2^0\}$ from $\mathbf{c}(0)$ to $\mathbf{c}(\tau)$. The value of θ is computed from the dot product of $\mathbf{c}(\tau) - \mathbf{x}$ with the vectors \mathbf{v}_1 and \mathbf{v}_2 as the angle from \mathbf{v}_1 in the range $[0, 2\pi]$. Note that, by construction, all three vectors are in the plane orthogonal to $\mathbf{t}(\tau)$ that contains $\mathbf{c}(\tau)$.

2.3 Encoding vessel anatomy

After defining the VCS, we will present several contexts in which it can be applied. In the first place, we discuss how the coordinates defined on a vessel section can be used to build a representation of the vessel itself. We address the development of patient specific models that are based on a common representation of the wall, making it easy to establish a correspondence between two individuals. We also benefit from the existence of this correspondence to build a convenient representation of a cohort of patients.

2.3.1 Patient specific vascular model

We start the process with segmented medical image data of the vessel and, more precisely, with a set of points on the vessel wall. We will take the common assumption that the vessel wall can be represented as a differentiable surface in the region of interest. Furthermore, we also assume that any section of the vessel, perpendicular to the vessel centerline, is a star-convex set: that is, all the points in the cross section can be seen from the centerline. Although this assumption imposes a limitation in some anatomical conditions, such as saccular aneurysms, it is still valid in a wide range of situations. Under this assumption, the radius of any point on the wall $\rho(\mathbf{x})$ can be expressed as a function of the other two coordinates of that point, $\rho(\mathbf{x}) = \rho_w(\tau(\mathbf{x}), \theta(\mathbf{x}))$. Then, using Eq. (4), the wall can be described as the surface defined by

$$\mathbf{x}(\tau, \theta) = \mathbf{c}(\tau) + \rho_w(\tau, \theta)(\mathbf{v}_1 \cos(\theta) + \mathbf{v}_2 \sin(\theta)), \quad (5)$$

for $\tau \in [0, 1]$, $\theta \in [0, 2\pi]$. Since the reference frame $\{\mathbf{v}_1, \mathbf{v}_2\}$ is defined for any τ from \mathbf{c} , in order to represent the anatomy of a patient it is enough to have a representation of \mathbf{c} and of ρ_w . Our proposal is to use a differentiable approximation by fitting a cubic spline curve for \mathbf{c} and a bivariate spline function for ρ_w .

We approximate the centerline \mathbf{c} as

$$\mathbf{c}(\tau) = \sum_{i=0}^n \mathbf{c}_i B_{\mathbf{t},i}(\tau) \quad (6)$$

where \mathbf{c}_i are 3-dimensional coefficients and $B_{\mathbf{t},i}$ are a basis of the space of B-Spline polynomials. The knot vector, $\mathbf{t} \in [0, 1]^{n+5}$, is a partition of the interval $[0, 1]$ and defines the region of influence of each $B_{\mathbf{t},i}$. We take \mathbf{t} as a uniform subdivision of $I = [0, 1]$, with $t_k = k/(n+4)$, $k = 0, \dots, n+4$, leading to so-called *uniform B-Splines*. From now on, vector \mathbf{t} will be assumed uniform and omitted in the notation for simplicity. The interested reader is addressed to the work by [Piegl and Tiller \(1996\)](#) for a detailed description of B-Splines. The approximation to the centerline is computed as the solution to a least squares problem on the coefficients \mathbf{c}_i , to minimize the difference from \mathbf{c} to the centerline points defined in Section 2.2.2.

For the wall, we get a sample of points on the surface of the vessel, and fit a uniform bivariate spline

$$\rho_w(\tau, \theta) = \sum_{i=0}^{n_1} \sum_{j=0}^{n_2} b_{ij} B_{ij}(\tau, \theta) \quad (7)$$

where $B_{i,j}(x, y) = B_i(x) \cdot B_j(y)$ and $(\tau, \theta) \in [0, 1] \times [0, 2\pi]$.

Finally, by using these spline approximations in Eq. (5), we represent the aorta wall as

$$\mathbf{x}(\tau, \theta) = \sum_{i=0}^n \mathbf{c}_i B_i(\tau) + \left[\sum_{i=0}^{n_1} \sum_{j=0}^{n_2} b_{ij} B_{ij}(\tau, \theta) \right] (\mathbf{v}_1 \cos(\theta) + \mathbf{v}_2 \sin(\theta)). \quad (8)$$

Fig. 3 shows the application of this approach to an aorta in our dataset.

This approach leads to a differentiable representation of the anatomy that uses a reduced number of real values; given values for n, n_1, n_2 , any vessel section is encoded using a vector with fixed dimension $m = 3n + n_1 \cdot n_2$, with the form

$$\mathbf{a} = (\mathbf{c}_0, \dots, \mathbf{c}_n, b_{00}, \dots, b_{n_1 n_2}) = (a_1, \dots, a_m). \quad (9)$$

Once the vessel has been characterized through the corresponding feature vector \mathbf{a} , an approximation of its original shape can be recovered by means of Eq. (8). The quality of this approximation will depend on the number of knots used for the different splines. To assess the quality of this approximation of the original wall, we will compute the patient specific model for all the aortas in our test cohort using different knot vectors, and compare the approximated wall with the original data. Given a point of the wall with Cartesian coordinates $\mathbf{p} = (x, y, z)$, we will compute its vessel coordinates $(\tau(\mathbf{p}), \theta(\mathbf{p}), \rho(\mathbf{p}))$, and define the residual of the approximation as

$$r(\mathbf{p}) = |\mathbf{p} - \mathbf{x}(\tau(\mathbf{p}), \theta(\mathbf{p}))|. \quad (10)$$

2.3.2 Coregistration of a cohort of vessels

A common preprocessing step when dealing with several samples of the same anatomy is geometry alignment or coregistration. Coregistration methods often rely on the alignment of a

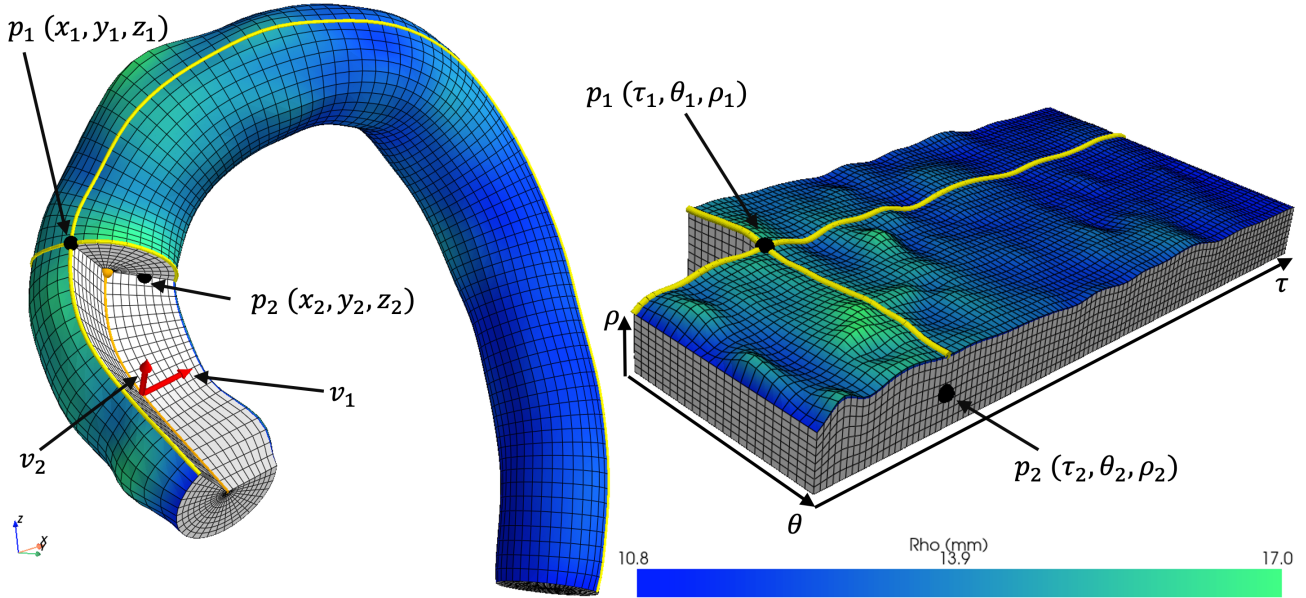


Figure 3: The representation of an aorta using the VCS. After computing the centerline of the vessel (in orange), the wall is approximated as a surface ρ_w depending on coordinates (τ, θ) . This surface is represented, on the right, in VCS space. The color map corresponds to the distance of the wall points to the centerline, in millimeters, with the radius ranging, for this aorta, from $\sim 10\text{mm}$ to $\sim 17\text{mm}$. Two points, p_0 (on the wall) and p_1 (inside the lumen) are represented in both Cartesian and VCS spaces, as well as two lines on the surface (in yellow), corresponding to $\theta = 5\pi/4$ and $\tau = 1/5$. The reference frame on the centerline is also shown in red in the Cartesian space for a point of the centerline.

set of points defined on the different anatomies. Ideally, there should be a one to one correspondence among these points on the different samples. However, in many cases it is not easy to define this correspondence beforehand, and specific numerical methods, such as Iterative Closest Point, are used. The patient specific model proposed here has two properties that make it useful for geometry coregistration.

In the first place, the construction of the VCS for every patient enables the definition of a set of equivalent alignment points on all the geometries. E.g., one can take points on the surface of the vessel forming a regular grid in the $\tau - \theta$ domain, with an automatic correspondence by definition. In the second place, the coefficients of the centerline have a geometrical meaning as control points. As a result, the application of a rigid transformation on these points results on the application of the transformation to the whole vessel anatomy.

Thus, when dealing with a set of geometries that require rigid coregistration, this step can be assisted by building the vascular models of all the anatomies before the alignment. The alignment can then be performed on a set of points built for this task with an explicit one to one correspondence, thanks to the vessel coordinate system. During the process, the resulting transform can be applied only to the centerline control points, without requiring the recomputation of the vessel model after every step.

2.3.3 Population representation and analysis

The set of functions that can be expressed by Eq. (8) form a vector space, isomorphic to the space of coefficient vectors defined in Eq. (9). This can be exploited to represent a particular phenotype as the combination of a reference shape plus a perturbation or deformation, making it very convenient for methods such as statistical shape modeling. Here, this idea will be developed by generating a population model on our cohort, using Principal Component Analysis (PCA).

If we have M vessel geometries, represented by their coefficients

$$\mathbf{a}^k = (c_0^k, \dots, c_n^k, b_{00}^k, \dots, b_{n_1 n_2}^k) = (a_1^k, \dots, a_m^k), \quad k = 1, \dots, M,$$

as defined in equations (8) and (9), each geometry can be represented by the mean vessel geometry, $\boldsymbol{\mu} = \sum_j \mathbf{a}^j / M$, plus the projection of its difference with $\boldsymbol{\mu}$ on the uncorrelated principal directions, \mathbf{u}_i

$$\mathbf{a} = \boldsymbol{\mu} + \sum_{i=0}^{m'} \alpha_i \mathbf{u}_i. \quad (11)$$

In this context, in which each \mathbf{u}_i can be interpreted as a change in shape that increases with α_i , the principal directions are also called variation or deformation modes.

We will compute the PCA of the aortas in our cohort and will explore the meaning of each deformation mode, to understand how the variation in shape within the cohort can be explained. By sampling the aortas' geometry at a set of fixed points, defined by their coordinates, we will quantify the deformation both of the centerline and of the width of the aorta under each deformation mode.

2.4 Application to inter-patient variability analysis

The VCS defines a one to one correspondence between points on two vessels, enabling the quantitative comparison of any field that is defined on its surface or inside its lumen. We will show this approach building an haemodynamic atlas based on Computational Fluid Dynamics (CFD) simulations on the cohort of aortas. For a quantitative comparison, we will define a common set of measurement points \mathbf{x}_i through their coordinates, and estimate on them the value of different quantities for all the vessel samples.

2.4.1 CFD simulation setup

For our computational blood flow simulations we will follow the approach by [Catalano et al. \(2021\)](#), considering rigid walls and steady state simulations with constant inflow boundary conditions in peak systole. We will assume the blood to be an incompressible, Newtonian fluid in laminar regime, with a kinematic viscosity of $3.37 \cdot 10^{-6} \text{ m}^2/\text{s}$. In all the aortas, we will impose comparable boundary conditions; a constant Dirichlet condition for the inlet velocity profile equal to 1.2 m/s, with an effective valve area of 1 cm^2 corresponding to a patient with aortic stenosis according to [Vahanian et al. \(2021\)](#); the standard no-slip condition, i.e. zero velocity Dirichlet condition, for the wall; and free outflow with null von Neumann boundary condition for the velocity at the outlet on the descending aorta. The open source framework OpenFOAM ([OpenFOAM Foundation](#)), version 10, will be used to solve the Navier-Stokes equations by means of the Finite Volume Method (FVM). We will generate the aorta wall in the form of a regular triangle mesh, using Eq. (8). This triangle mesh will be used as the input of the snappyHexMesh software provided with OpenFOAM, to generate hexa-dominant volume computational meshes. The SIMPLE algorithm will be used to approximate the solution, assuming convergence when residuals fall below 10^{-5} . It is noteworthy that the simulations have not been physiologically validated, since their purpose is to serve as a use case of the VCS. Hence, no biophysical conclusions should be taken from the results.

2.4.2 Haemodynamic atlas on the aorta

We will build the haemodynamic atlas following an approach similar to the analysis of anatomy in Section 2.3.3. We perform a CFD simulation for each of the vessels in the cohort and, in this case, we compute a PCA for each one of the flow variables across the cohort. This strategy is usually hindered by the fact that the computational grids of two vessels cannot be compared directly. Moreover, it is not straightforward to define measurement points on which perform the desired comparison. By means of the VCS, a comparable measurement grid will be generated for all the aortas, considering the correspondence defined by the coordinate values. To ease the notation, we will normalize the radial coordinate; given a point \mathbf{x} with coordinates (τ, θ, ρ) , we define $\rho_n(\mathbf{x}) = \rho/\rho_w(\tau, \theta)$. This normalized coordinate is always in the range $[0, 1]$ for a point inside the aorta, with $\rho_n = 0$ still representing points located on the centerline, while $\rho_n = 1$ now corresponds to points on the wall. Then, we will build a regular grid in the region $\Omega = [0, 1] \times [0, 2\pi] \times [0, 1]$ and use the resulting points to measure the quantities of interest on the resulting points of every aorta from the computed CFD solution. As a result, every aorta will have a comparable vector of measurements that allows quantitative comparison.

For our atlas, we will focus on pressure, velocity and wall shear stress (the later only defined for points on the wall). For each one of these fields, a separate PCA has been performed; the average dynamics will be computed within the cohort, and the principal uncorrelated modes of variation of the flow will be studied, showing the most significant differences observed.

3 Results

Next we present the results of the different experiments proposed. Following the structure of Section 2, we start with the analysis of the patient specific model as a tool to approximate the vessel wall. Then, we present the results of the statistical shape analysis of the available cohort, and conclude with the construction of an haemodynamic atlas for this set of aortas.

3.1 Patient specific model

As described in Section 2.3.1, the parametric model of a vessel defined by Eq. (8) depends on the size of the knot vectors, that control the degrees of freedom of the B-Splines. We will denote by L the number of knots for τ in the approximation of \mathbf{c} . K and R will be, respectively, the number of knots for τ and θ in the approximation of ρ_w . The quality of the approximation of the parametric surface given by Eq. (8) has been measured for each aorta using the residual r defined in Eq. (10). This results in a distribution of r for each aorta across its surface.

The approximation of the wall is a smooth surface that can reproduce very closely the input data. In Fig. 4 we can find, in the upper row, from left to right, the input triangle mesh for one of the aortas, the B-Spline approximation using $L = 9$, $R = 15$ and $K = 19$, and both geometries superimposed (the approximation in blue). The lower row of the figure shows the distribution of the residuals for that case, with two close-up images corresponding to the regions with less approximation precision; around the sinuses of Valsalva and the upper wall of the aortic arch. Note that the value of the residuals distributes uniformly except for the highlighted regions and that, even there, the highest value of the residuals is around 1mm.

To test the convergence of the patient specific model and the effect of L , R , and K on the residuals, we have carried out a sensitivity analysis. For each aorta, \mathbf{a}^k , we have computed the mean residual, \bar{r}^k , and, in order to detect the existence of regions where the approximation could be less precise, the 75th quantile of the distribution, r_{75}^k . Finally, we have averaged these two indicators across the samples in the cohort. Next, we present the results for values of L , K and R in the range from 5 to 19.

In Fig. 5 the results of the analysis are presented in the form of isosurfaces of error, i.e., each surface represents the region in the space of parameters (R, L, K) that correspond to a fixed value of the residual, encoded in the surface color. The results indicate that the parameter that has a highest influence in residual reduction is the number of knots for the surface in the longitudinal direction, K . Note that, the closer the surfaces are, the higher is the residual gradient with respect to the parameter in that direction. Thus, the surfaces that are closely stacked at the bottom of the plot imply that, when K is low, an increase of knots in that direction yield higher error reduction. On the contrary, the rate of improvement decays as K increases, indicating convergence.

Given a value of K , the error is very stable w.r.t. the other two parameters, R and L . This has a practical implication; given a value of K , which will govern the quality of the approximation, there is a reasonably wide range of values for both L and R that lead to a similar behavior. This means that, from the user perspective, tuning of the parameters is straightforward.

We only observe an increase of error for very small or very large number of knots in the centerline approximation, L . The

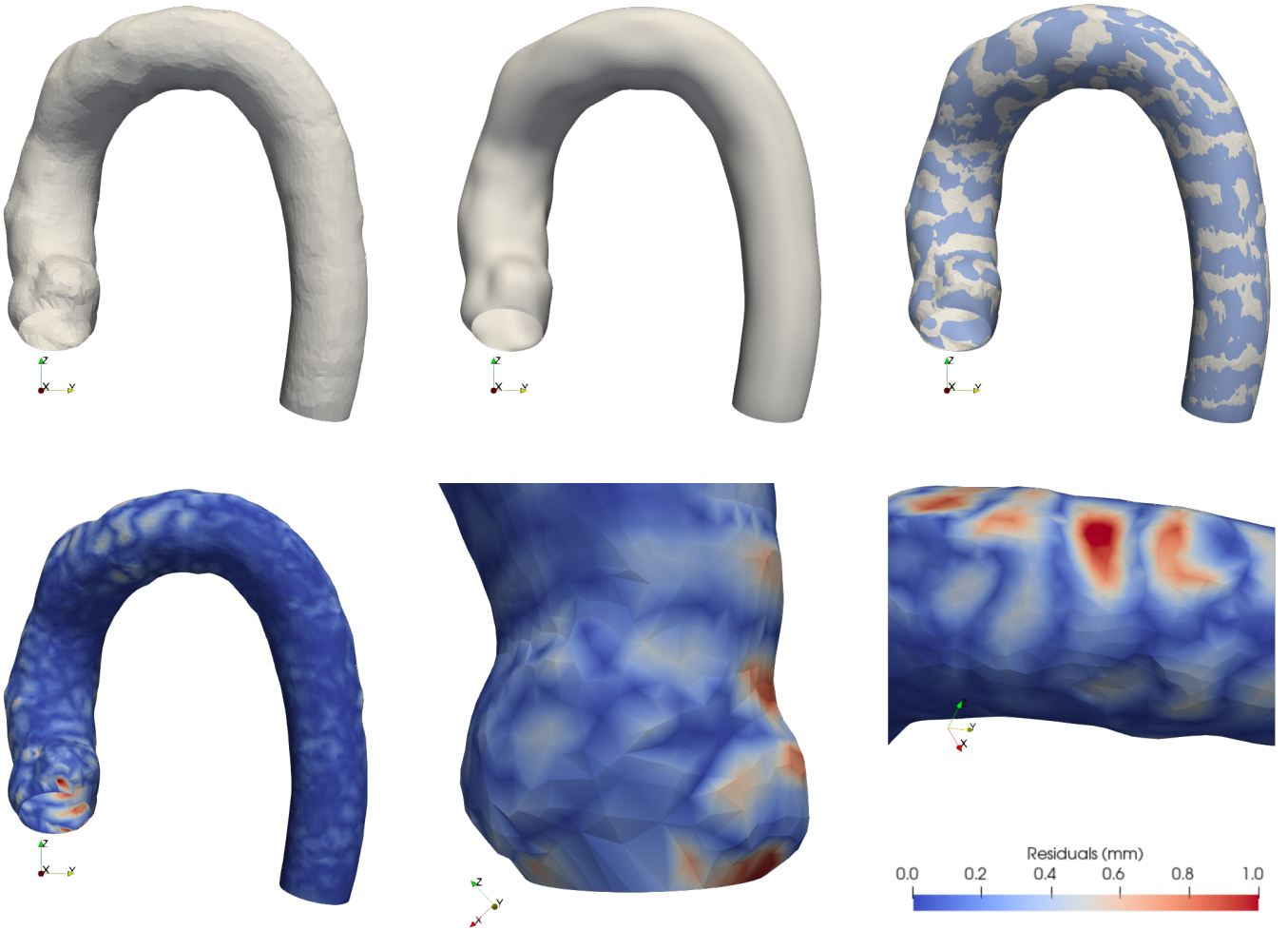


Figure 4: On the first row, from left to right, the input aorta, the patient specific B-Spline approximation using $L = 9, R = 15, K = 19$, and the superimposition of both (the approximation light blue). On the second row, the distribution of residuals (in mm) on the input mesh, with detailed views of the sinuses of Valsalva and the aortic arch, where the approximation is less accurate.

error at low values of L is due to the lack of degrees of freedom to properly approximate c . On the contrary, when L reaches 19, an excessive adaption of c to the sampling used to mark the centerline region (see Section 2.2.2) leads to a wiggling centerline curve, which translates into light oscillation on the wall. Nevertheless, when this effect is most noticeable, the error is still at its minimum values.

The plot on the bottom of Fig. 5 corresponds to isosurfaces of error at the 75th quantile of the error distribution (averaged across the cohort). That is, it explains the behavior of the error in the regions corresponding to the upper tail of the error distribution. In this case, we see that low values of R have a negative influence, specially at high values of L . Our interpretation is that, when the aforementioned wiggling effect appears in the centerline, small resolution in the traversal direction of the surface leads to a less accurate adaption to the observed data.

3.2 Population analysis

We have obtained the patient specific model for each of the 30 aortas in our cohort for $L = 9, R = 15$ and $K = 19$. Then, we have performed a PCA on the resulting set of feature vectors, obtaining the mean aorta and the principal directions. Note that, if the number of points used during the PCA, N , is lower than

the dimension of the space, the number of nonzero principal directions will be N , except for degenerate cases. Thus, in our case, the PCA will yield 30 principal directions. Fig. 6 shows the mean geometry obtained after the PCA. As it can be expected, the average geometry is a very smooth surface, without any particular protuberance. It is noteworthy that the sinuses of Valsalva have been captured in the mean aorta. This indicates that the VCS proposed is consistent across individuals, and that the derived point correspondence is properly defined.

The VCS allows a separate analysis for the centerline and the wall of the vessel. Fig. 7 presents a graphical comparison of the first 5 deformation modes obtained by the PCA. For each deformation mode, \mathbf{u}_i , the figure shows the wall of the aortas $\mu \pm 2\sigma_i \mathbf{u}_i$, where σ_i is the observed variance of the cohort along that direction. Each deformed wall is shown in saggital and coronal view, superimposed with a phantom of the mean aorta, for comparison. In addition, the deformed centerline is also shown compared to the centerline of the mean aorta. Using the one to one correspondence between points on two vessels, defined by the VCS, differences between the mean shape and the deformed anatomy have been computed and represented using a color scale.

In the case of the wall, the difference in the radius of the aorta is represented for each point. This shows, e.g., how the first deformation mode is responsible for a narrowing or widening

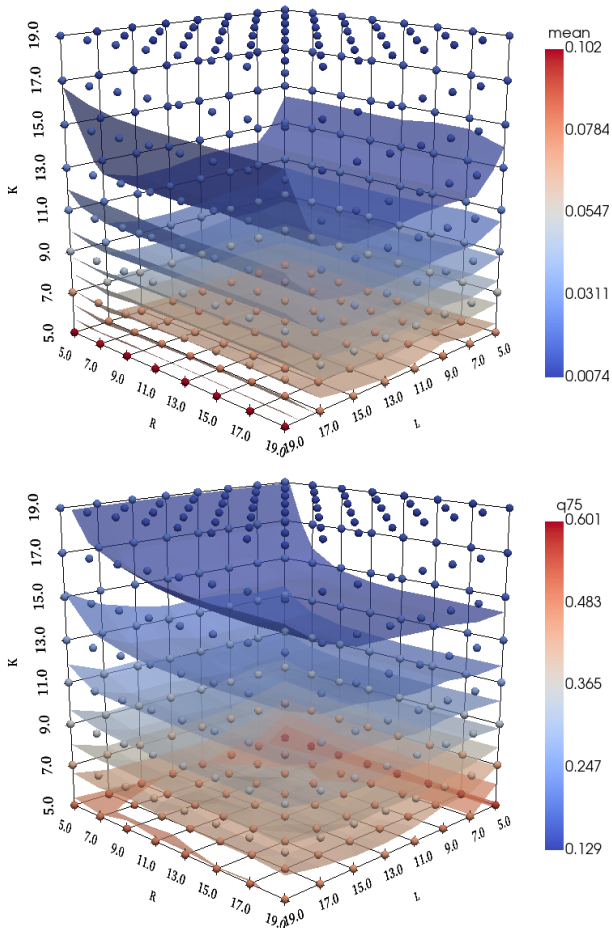


Figure 5: Plot of the sensitivity analysis on the influence of the parameters L , R , and K over the estimation residuals of the patient specific vascular model. The top plot shows the cohort average of the mean residuals, and the bottom plot shows the cohort average of the 75th quantile of the residuals, in both cases expressed in millimeters. In both plots, the dots placed in a regular grid are color-coded to indicate the value of the residual at the corresponding values of L , R and K .

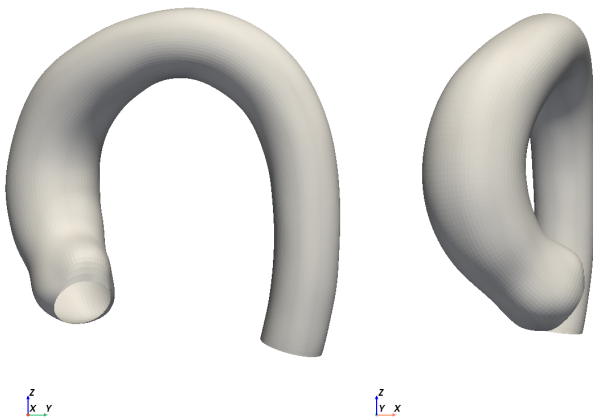


Figure 6: The sagittal and coronal views of the mean thoracic aorta geometry obtained as a result of the PCA.

of the whole lumen, while the second mode of variation has an opposite effect on ascending and descending sections. The other three modes represented have more local effects, as in the fourth mode where the main variations can be observed in the sinuses of Valsalva and the sinotubular junction, or in the fifth mode, that affects the ascending aneurysm anatomy.

The warping of the centerline has been measured as the \mathbb{R}^3 euclidean distance between points with the same value of τ on the mean and the deformed curves. The representation of the deformation enables an easy inspection of the regions affected by each deformation mode. This way, we see how the third mode of deformation has a rather uniform effect on the whole curve, while the rest of modes cause more local displacements. It has to be noted that the distances in the plot can appear smaller than they actually are due to the projection. This analysis shows that, in our cohort, the variation of shape can be described mainly by the deformation of the distal part of the aortic arch (first deformation mode) and by the flatness of the arch (second mode of variation) and by the vertical roundness of the global shape (fifth mode of variation). It is also noteworthy that two of the five deformation modes (the second and fourth modes) have little impact on the centerline shape, with effect mainly on the wall radius.

3.3 Haemodynamic atlas

A CFD simulation has been performed on every aorta using the finite volume method, as described in Section 2.4.2. Fig. 8 shows the average fields, measured on the cohort, for the three quantities inspected. Velocity is plotted, in the first row of the figure, over a regular internal grid on the mean geometry obtained in Section 3.2. The left figure presents the magnitude of the vector field. To show the interior of the fluid, the volume is clipped using a threshold in the coordinate θ of the aorta lumen, and the value is shown on the resulting surfaces. This kind of plot, which cannot be done by merely clipping the volume using planes, becomes extremely easy thanks to the VCS. In the right figure, the first row presents streamlines integrated along this field. In a similar fashion, the second row presents the value of pressure over the same grid. In this case, the right plot presents the value of pressure on the wall from a posterior view. Finally, the third row presents wall shear stress, which is only defined on the wall, from the anterior and posterior views.

As in the case of the anatomy, where the sinuses of Valsalva were captured by the mean geometry, the mean flow presents traits that are characteristic to the flow of the individual aortas. This, again, points towards a proper point correspondence between individuals that helps to capture the characteristics of the flow at each different region of the aorta.

The use of the VCS as a tool for measuring and visualizing data in a vessel also helps to inspect the variation of the flow within the cohort. In Fig. 9, the first mode of variation of the three flow fields of interest is shown. In this case, the plot shows the first principal component multiplied by $2\sigma_1$. Only the positive increment has been included, since the flow difference using $-2\sigma_1$ would simply invert the colors of the plot.

The figure is presented in three rows and four columns; each row corresponding to a variable of the flow; and the two first columns correspond to ventral view, while the two later columns correspond to dorsal view of the aorta. In first and third columns, the value of flow is represented in the regular mesh built using the VCS for field evaluation. In the case of the velocity (first row) the grid is clipped using the coordinate θ , to enable inspection of the lumen, as in Fig. 8. In the second and fourth columns, the mesh is clipped using the value of the variable of interest. That is, the cells with a value in the upper 20% of the observed range are shown, to highlight which

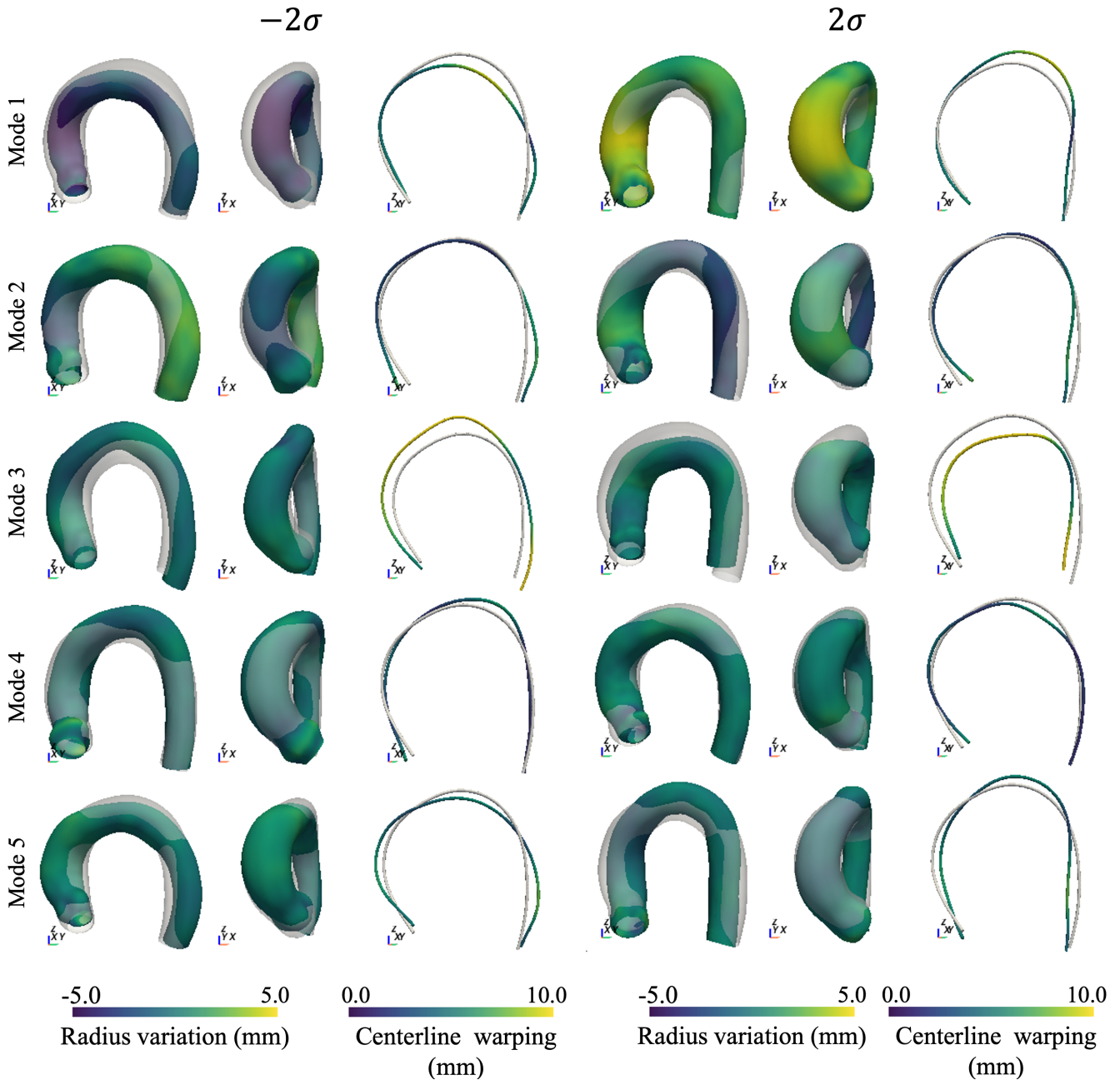


Figure 7: The illustration of the five deformation modes. Deformation modes, are sorted from top to bottom, then the first three columns are the negative deformation and the last three the positive. The deformation of each mode is split in the contribution of the centerline and the radius function. The gray phantom shape corresponds to the mean aorta in both surface and centerline.

are the main areas of influence of the the principal component. These regions correspond, thus, to the regions of the aorta in which higher variability is shown across the cohort.

4 Discussion

We have defined a coordinate system that adapts to vessel anatomy, and allows the unambiguous identification of a point in both the lumen and the wall. This enables the definition of a correspondence between the anatomy of different patients, with applications to inter-patient comparison, quantitative cohort analysis or patient specific data aggregation. The computation of the VCS and the derived methods only requires the identification of the vessel segment of interest and the definition of a reference frame for one of the two ends. Thus, once the region of interest has been segmented, it is a completely au-

tomatic process which takes less than a couple of minutes for a thoracic aorta on a standard desktop PC.

The coordinates of a point are well defined as long as Eq. (1) has a unique solution, which is met for the set Ω of the points that are closer to c than the curvature radius of the centerline. Thus, the VCS can be computed in the region of points that are close enough to the curve according to this criterion. In the vast majority of cases, this region will include the complete vessel lumen. The VCS has been tested on the aortic arches of a cohort of patients with ascending aorta aneurysm. This scenario includes large vessel radius sections, and, in all the cases, the whole vessel was within Ω . Nevertheless, when computing the centerline this condition can be forced during the application of the A^* algorithm (Section 2.2.2).

The proposed coordinate system generalizes other comparable approaches that use cylindrical coordinates for vessels.

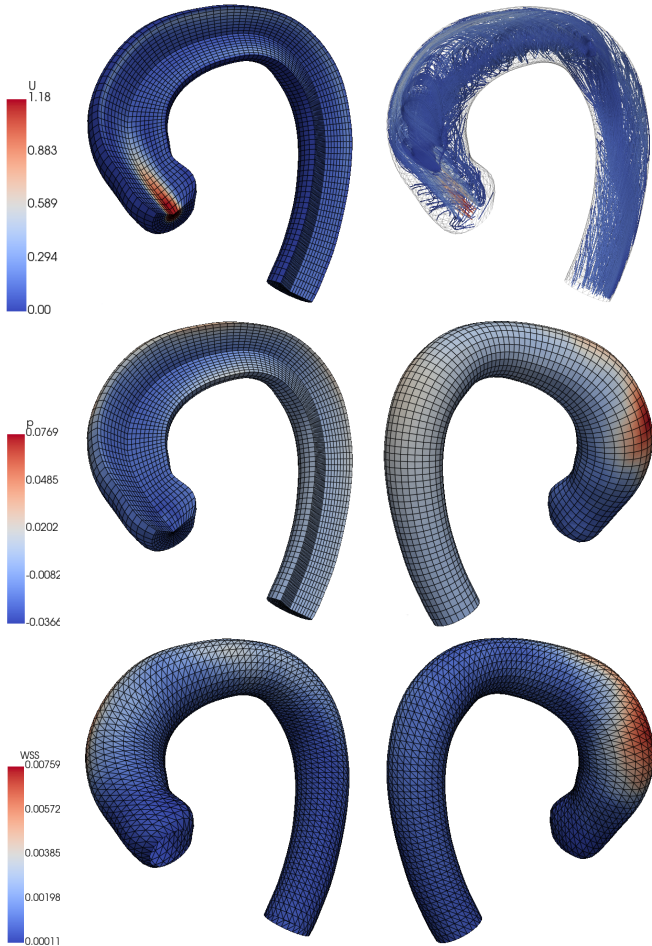


Figure 8: Using the VCS, a grid is used to evaluate the flow on all the aortas of the cohort and, then averaged. The result is represented over the average anatomy. From top to bottom, velocity (m/s), pressure (Pa) and wall shear stress (m^2/s^2). The internal mesh corresponds to the measurement points, and not to the computational grid used for CFD simulation.

Bersi et al. (2016, 2019) use a straight line segment as the longitudinal direction, while Meister et al. (2020) rely on the Frenet frame for the centerline. This limits their scope to work with nearly straight vessel segments, which is an impractical requirement at large regions of the vascular system. The generalization of the longitudinal axis by a longitudinal curve, and the parallel transport frame used in our proposal allow to overcome this limitation. Our approach also generalizes the concept of canal surfaces, that consider circular or elliptical cross sections (Alvarez et al., 2017; Antiga et al., 2008; Piccinelli et al., 2009), allowing the construction of accurate patient specific models. Guo et al. (2013) and Ghaffari et al. (2017) propose comparable approaches, but limit their work to mesh generation, while our definition of vessel coordinates enables inter- and intra-patient point to point correspondence.

The patient specific vascular model built upon the VCS involves a very reduced number of parameters (L , K and R) which, according to our tests, are easy to choose; we have found that the approximation error for our cohort is clearly below the usual medical imaging resolution, and that the quality of the adjustment can be controlled just by increasing L for a good range of values of the other parameters. Our approach is less general than other strategies that serve for arbitrary surfaces (Bruse et al., 2016, 2017; Sophocleous et al., 2018), but its computa-

tion is very fast, taking barely a few seconds once the VCS has been obtained. In addition, the representation based on B-Splines coefficients is very intuitive thanks to its geometrical interpretation.

The model is low dimensional, compared to the equivalent medical image or triangle mesh surface data; a few hundred floating point values are enough to achieve a very good approximation for the aorta anatomy. All the samples in a cohort have the same dimension, with comparable feature vectors, which is most often a requirement for any statistical or machine learning analysis (Bruse et al., 2017; Liang et al., 2020; Meister et al., 2020; Niederer et al., 2020; Sophocleous et al., 2018). Using this property, the anatomical variability of our cohort is analyzed by means of a PCA on the set of patients’ feature vectors of B-Spline coefficients, as shown in Section 3.2. Note that this analysis can also be done for different CT or MRI scans of a single patient. This would enable temporal analysis of cardiac cycle or assessment of disease evolution along time, e.g., to evaluate aneurysm growth.

Our results are consistent with other shape variability analyses, indicating the importance of modes that affect the diameter of the aorta and the arch shape (Casciaro et al., 2014; Catalano et al., 2021; Ou et al., 2007). In addition, we use the point-to-point correspondence on the surface of the vessels, and the explicit consideration of the centerline in the patient specific model, to perform a more insightful analysis. When a deformation is represented combining the arch and wall displacements, it can be difficult to clearly understand how much of the displacement comes from the arch shape distortion and how much is due to diameter changes. However, we are able to show the arc shape variation with the deformed centerline and quantify the amount of wall displacement w.r.t. that centerline in the resulting shape, as shown in Fig. 7. This helps a better identification of the regions that are actually affected by diameter changes. This ability to separate the variation of shape in the centerline and in the wall diameter can give insight on how anatomy at different scales correlates with clinical condition (Wu et al., 2019; Lovato et al., 2024).

Geometric consistency across patients has been reported as a relevant property for anatomy representation, both for obtaining valid large deformations (Catalano et al., 2021) and for avoiding spurious deformations in the principal variation modes (Thamsen et al., 2021). It is remarkable that, in the mean aorta, the sinuses of Valsalva are observable, indicating the inter-patient consistency of the vessel coordinate system. The mean flow of the haemodynamic atlas shown in Section 3.3 points in the same direction, since features such as the helicity along the aortic arch or the WSS profile in the ascending aorta aneurysm have not been smoothed away due to coordinate mismatches between patients.

The haemodynamic atlas built in Section 3.3 differs from that of Catalano et al. (2021) in the sense that they run their CFD simulations on the shapes resulting from the deformation modes, while we perform them on the original cohort. Thamsen et al. (2021) also run the simulations on the cohort, but they do not perform a variability analysis. Instead, they compare pressure measured along the centerline. We exploit the VCS to build an internal measurement mesh, equivalent for all the aortas, and apply a PCA on the resulting numerical values. This provides powerful visualization approaches, as shown in Figs. 8 and 9.

In our CFD setup, the wall was considered rigid. However,



Figure 9: From top to bottom, the first principal component of the velocity, U , (m/s), pressure (Pa) and wall shear stress (m^2/s^2). The solid mesh for velocity is displayed open to show the interior of the lumen. The second and fourth columns present the regions where the variation is at least a 20% from the total maximum variation. The meshes used in the figures are not the CFD computational meshes but a regular grid built using the VCS for visualization.

if fluid-structure interaction (FSI) is used to account for wall deformation, the measurement mesh will automatically adapt to the deformed shape, requiring no additional computation. Moreover, in FSI simulations, wall representation as a polynomial surface enables the application of isogeometric analysis (Zhang et al., 2007) and can help describe heterogeneous wall properties by describing them in the $\tau - \theta$ space.

Moreover, the proposed representation for anatomy and flow is well suited for its use in statistics and machine learning methods (Liang et al., 2020), enabling quantitative analysis in the complete lumen and the wall. In a very preliminary analysis, we have found the ability to predict some flow variation modes from the first 20 deformation modes using linear regression. As expected, pointwise prediction of the flow has not been achieved for the whole aorta, but, remarkably, there exists regions in which even linear regression still yields good results.

The presented methodology to encode flow fields offers a new approach to diverse problems, such as the combination of data from different sources, for instance combining 4D flow MRI with numerical simulations, to impose boundary conditions, to validate in both directions, or to tackle the denoising problem (Fathi et al., 2020). VCS coordinates on the wall can also be used to describe the distribution of mechanical properties if tissue or wall thickness, taking the same approach applied to build the haemodynamics atlas. Moreover, the standard formatting of the encoding makes it appropriate as the in-

put for machine learning techniques. With a different encoding method this approach was used by Liang et al. (2020), where the authors predicted the main flow fields and analyzed the feasibility of using said predictions in clinical application.

In the context of the development of the digital twin, our proposal can serve as a robust and versatile vessel encoding method, that covers both anatomy and biophysical data. Although not tested in this work, its utility for aggregating data from different sources is clear, and we also think that it can help to find anatomical landmarks. Moreover, the fact that the description proposed is differentiable makes it adequate for differentiable programming (Xie et al., 2023) or uncertainty quantification (Perinajová et al., 2021; Rego et al., 2021).

A limitation of the VCS is that it cannot deal with vessel branching. Vessel bifurcations are regions of great interest, since atherosclerotic plaques develop around them and they can have great impact on flow dynamics. Nevertheless, this problem can be overcome, with some effort, by applying the VCS to each vessel section and building a vessel tree with existing methods for branching description (Antiga and Steinman, 2004; Ghaffari et al., 2017; Guo et al., 2013; Medrano-Gracia et al., 2016). The election of uniform B-Splines helps to establish the point correspondence between vessels. This, however, can lead to artifacts if the vessels have several sections with specific characteristics but with variable length. A proper reparametrization of c can help in this situations, by imposing

certain values of τ at the landmarks of interest.

5 Conclusions

We have defined a vessel coordinate system that allows the unambiguous identification of locations in a vessel segment. We have described the technical details necessary for its computation, discussing the main assumptions taken and how they guarantee a proper definition. To show the applications of our proposal, we have analyzed the anatomical variability of a cohort of thoracic aortas and built an haemodynamic atlas. The VCS has been used at different stages to enable geometry encoding, quantitative comparison, flow variability analysis and advanced visualization. Although some further advancements are yet to be developed, specially to introduce branching structures, the proposed methods could serve as a robust piece for vascular modeling in the development of the digital twin.

Author contributions

PR, ML and IGF Conceptualized the vessel coordinate system, its applications and the code involving its computation. PR and AP, designed and carried out the blood flow simulations. PR, ML and IGF designed and developed the code involving the visualization and graphic material. PR, RS, ML and IGF wrote the original draft. RS and IGF acquired the funds to carry out the work.

Conflict of interest statement

The authors declare that they have no known competing financial interests or personal relationships that could have appeared to influence the work reported in this paper.

Acknowledgements

This work was funded by Generalitat Valenciana Grant AICO/2021/318 (Consolidables 2021) and Grant PID2020-114291RB-I00 funded by MCIN/ 10.13039/501100011033. None of the sponsors were involved in any step of the execution of the study or the preparation of the manuscript. The authors would like to thank Laia Romero for her advice in the generation of graphical material.

References

Mark Alber, Adrian Buganza Tepole, William R. Cannon, Suvransu De, Salvador Dura-Bernal, Krishna Garikipati, George Karniadakis, William W. Lytton, Paris Perdikaris, Linda Petzold, and Ellen Kuhl. Integrating machine learning and multiscale modeling—perspectives, challenges, and opportunities in the biological, biomedical, and behavioral sciences. *NPJ Digital Medicine*, 2(1), nov 2019. URL <https://dx.doi.org/10.1038/s41746-019-0193-y>.

Luis Alvarez, Agustín Trujillo, Carmelo Cuenca, Esther González, Julio Esclarín, Luis Gomez, Luis Mazorra, Miguel Alemán-Flores, Pablo G Tahoces, and José M Carreira. Tracking the aortic lumen geometry by optimizing the 3d orientation of its cross-sections. In *International Conference on Medical Image Computing and Computer-Assisted*

Intervention, pages 174–181. Springer, 2017. URL https://doi.org/10.1007/978-3-319-66185-8_20.

- L. Antiga and D. A. Steinman. Robust and objective decomposition and mapping of bifurcating vessels. *IEEE Transactions on Medical Imaging*, 23(6):704–713, 2004. URL <https://doi.org/10.1109/TMI.2004.826946>.
- Luca Antiga, Marina Piccinelli, Lorenzo Botti, Bogdan Ene-Iordache, Andrea Remuzzi, and David A. Steinman. An image-based modeling framework for patient-specific computational hemodynamics. *Medical & Biological Engineering & Computing*, 46(11):1097, 2008. ISSN 1741-0444. URL <https://doi.org/10.1007/s11517-008-0420-1>.
- Ruth E. Baker, Jose-Maria Peña, Jayaratnam Jayamohan, and Antoine Jérusalem. Mechanistic models versus machine learning, a fight worth fighting for the biological community? *Biology Letters*, 14(5):20170660, 2018. URL <https://dx.doi.org/10.1098/rsbl.2017.0660>.
- Jason Bayer, Anton J. Prassl, Ali Pashaei, Juan F. Gomez, Antonio Frontera, Aurel Neic, Gernot Plank, and Edward J. Vigmond. Universal ventricular coordinates: A generic framework for describing position within the heart and transferring data. *Medical Image Analysis*, 45:83–93, 2018. ISSN 1361-8415. URL <https://doi.org/10.1016/j.media.2018.01.005>.
- Jason D Bayer, Robert C Blake, Gernot Plank, and Natalia A Trayanova. A novel rule-based algorithm for assigning myocardial fiber orientation to computational heart models. *Annals of biomedical engineering*, 40:2243–2254, 2012.
- Matthew R. Bersi, Chiara Bellini, Paolo Di Achille, Jay D. Humphrey, Katia Genovese, and Stéphane Avril. Novel Methodology for Characterizing Regional Variations in the Material Properties of Murine Aortas. *Journal of Biomechanical Engineering*, 138(7), 06 2016. ISSN 0148-0731. URL <https://doi.org/10.1115/1.4033674>. 071005.
- Matthew R. Bersi, Chiara Bellini, Jay D. Humphrey, and Stéphane Avril. Local variations in material and structural properties characterize murine thoracic aortic aneurysm mechanics. *Biomechanics and Modeling in Mechanobiology*, 18(1):203–218, February 2019. ISSN 1617-7959, 1617-7940. URL <https://doi.org/10.1007/s10237-018-1077-9>.
- Richard L. Bishop. There is more than one way to frame a curve. *The American Mathematical Monthly*, 82(3): 246–251, 1975. URL <https://doi.org/10.1080/00029890.1975.11993807>.
- Harry Blum. A Transformation for Extracting New Descriptors of Shape. In W. Wathen-Dunn, editor, *Models for the Perception of Speech and Visual Form*, pages 362–380. MIT Press, 1967.
- Jan L. Bruse, Kristin McLeod, Giovanni Biglino, Hopewell N. Ntsinjana, Claudio Capelli, Tain-Yen Hsia, Maxime Sermesant, Xavier Pennec, Andrew M. Taylor, Silvia Schievano, Andrew Taylor, Alessandro Giardini, Sachin Khambadkone, Marc de Leval, T. Y. Hsia, Edward Bove, Adam Dorfman,

- G. Hamilton Baker, Anthony Hlavacek, Francesco Migliavacca, Giancarlo Pennati, Gabriele Dubini, Alison Marsden, Jeffrey Feinstein, Irene Vignon-Clementel, Richard Figliola, John McGregor, and for the Modeling of Congenital Hearts Alliance (MOCHA) Collaborative Group. A statistical shape modelling framework to extract 3d shape biomarkers from medical imaging data: assessing arch morphology of repaired coarctation of the aorta. *BMC Med Imaging*, 16(1):40, 05 2016. ISSN 1471-2342. URL <https://doi.org/10.1186/s12880-016-0142-z>.
- Jan L Bruse, Maria A Zuluaga, Abbas Khushnood, Kristin McLeod, Hopewell N Ntsinjana, Tain-Yen Hsia, Maxime Sermesant, Xavier Pennec, Andrew M Taylor, and Silvia Schievano. Detecting clinically meaningful shape clusters in medical image data: Metrics analysis for hierarchical clustering applied to healthy and pathological aortic arches. *IEEE Trans Biomed Eng*, 64(10):2373–2383, 10 2017. URL <https://doi.org/10.1109/TBME.2017.2655364>.
- Daniel Carroll, Emek Köse, and Ivan Sterling. Improving frenet’s frame using bishop’s frame. arXiv, 2013. URL <https://doi.org/10.48550/ARXIV.1311.5857>.
- Mariano E Casciaro, Damian Craiem, Gilles Chironi, Sebastian Graf, Laurent Macron, Elie Mousseaux, Alain Simon, and Ricardo L Armentano. Identifying the principal modes of variation in human thoracic aorta morphology. *Journal of thoracic imaging*, 29(4):224–232, 2014. URL <https://doi.org/10.1097/RTI.000000000000060>.
- Chiara Catalano, Valentina Agnese, Giovanni Gentile, Giuseppe Raffa, Michele Pilato, and Salvatore Pasta. Atlas-based evaluation of hemodynamic in ascending thoracic aortic aneurysms. *Applied Sciences*, 12:394, 12 2021. URL <https://doi.org/10.3390/app12010394>.
- Jorge Corral-Acero, Francesca Margara, Maciej Marciniak, Cristobal Rodero, Filip Loncaric, Yingjing Feng, Andrew Gilbert, Joao F Fernandes, Hassaan A Bukhari, Ali Wajdan, Manuel Villegas Martinez, Mariana Sousa Santos, Mehrdad Shamohammdi, Hongxing Luo, Philip Westphal, Paul Leeson, Paolo DiAchille, Viatcheslav Gurev, Manuel Mayr, Liesbet Geris, Pras Pathmanathan, Tina Morrison, Richard Cornelussen, Frits Prinzen, Tammo Delhaas, Ada Doltra, Marta Sitges, Edward J Vigmond, Ernesto Zacur, Vicente Grau, Blanca Rodriguez, Espen W Remme, Steven Niederer, Peter Mortier, Kristin McLeod, Mark Potse, Esther Pueyo, Alfonso Bueno-Orovio, and Pablo Lamata. The ‘digital twin’ to enable the vision of precision cardiology. *Eur Heart J*, 41(48):4556–4564, 12 2020. URL <https://doi.org/10.1093/eurheartj/ehaa159>.
- Federica Cosentino, Giuseppe M Raffa, Giovanni Gentile, Valentina Agnese, Diego Bellavia, Michele Pilato, and Salvatore Pasta. Statistical shape analysis of ascending thoracic aortic aneurysm: Correlation between shape and biomechanical descriptors. *Journal of Personalized Medicine*, 10(2), Apr 2020. ISSN 2075-4426. URL <https://doi.org/10.3390/jpm10020028>.
- Stanley Durrleman, Xavier Pennec, Alain Trouvé, and Nicholas Ayache. Statistical models of sets of curves and surfaces based on currents. *Medical Image Analysis*, 13(5):793 – 808, 2009. ISSN 1361-8415. URL <https://doi.org/10.1016/j.media.2009.07.007>. Includes Special Section on the 12th International Conference on Medical Imaging and Computer Assisted Intervention.
- Mojtaba F. Fathi, Isaac Perez-Raya, Ahmadreza Baghaie, Philipp Berg, Gabor Janiga, Amirhossein Arzani, and Roshan M. D’Souza. Super-resolution and denoising of 4d-flow mri using physics-informed deep neural nets. *Computer Methods and Programs in Biomedicine*, 197:105729, 2020. ISSN 0169-2607. URL <https://doi.org/10.1016/j.cmpb.2020.105729>.
- Leonardo Geronzi, Antonio Martinez, Michel Rochette, Kexin Yan, Aline Bel-Brunon, Pascal Haigron, Pierre Escriq, Jacques Tomasi, Morgan Daniel, Alain Lalande, Siyu Lin, Diana Marcela Marin-Castrillon, Olivier Bouchot, Jean Porterie, Pier Paolo Valentini, and Marco Evangelos Biancolini. Computer-aided shape features extraction and regression models for predicting the ascending aortic aneurysm growth rate. *Computers in Biology and Medicine*, 162:107052, 2023. ISSN 0010-4825. URL <https://doi.org/10.1016/j.compbiomed.2023.107052>.
- Mahsa Ghaffari, Kevin Tangen, Ali Alaraj, Xinjian Du, Fady T. Charbel, and Andreas A. Linninger. Large-scale subject-specific cerebral arterial tree modeling using automated parametric mesh generation for blood flow simulation. *Computers in Biology and Medicine*, 91:353–365, 2017. ISSN 0010-4825. URL <https://doi.org/10.1016/j.compbiomed.2017.10.028>.
- Debora Gil, Ruth Aris, Agnès Borrás, Esmitt Ramírez, Rafael Sebastian, and Mariano Vazquez. Influence of fiber connectivity in simulations of cardiac biomechanics. *International journal of computer assisted radiology and surgery*, 14:63–72, 2019. URL <https://doi.org/10.1007/s11548-018-1849-9>.
- Jixiang Guo, Shun Li, Yim Pan Chui, Jing Qin, and Pheng Ann Heng. Mesh quality oriented 3d geometric vascular modeling based on parallel transport frame. *Computers in Biology and Medicine*, 43(7):879–888, 2013. ISSN 0010-4825. URL <https://doi.org/10.1016/j.compbiomed.2013.04.004>.
- Pablo Lamata. Teaching cardiovascular medicine to machines. *Cardiovascular Research*, 114(8):e62–e64, 2018. URL <https://doi.org/10.1093/cvr/cvy127>.
- Liang Liang, Minliang Liu, Caitlin Martin, John A. Elefteriades, and Wei Sun. A machine learning approach to investigate the relationship between shape features and numerically predicted risk of ascending aortic aneurysm. *Biomechanics and Modeling in Mechanobiology*, 16(5):1519–1533, Oct 2017. ISSN 1617-7940. URL <https://doi.org/10.1007/s10237-017-0903-9>.
- Liang Liang, Minliang Liu, Caitlin Martin, and Wei Sun. A machine learning approach as a surrogate of finite element analysis-based inverse method to estimate the zero-pressure geometry of human thoracic aorta. *International Journal for Numerical Methods in Biomedical Engineering*, 34(8):e3103, 2018. URL <https://doi.org/10.1002/cnm.3103>. e3103 CNM-Dec-17-0318.

- Liang Liang, Wenbin Mao, and Wei Sun. A feasibility study of deep learning for predicting hemodynamics of human thoracic aorta. *J Biomech*, 99:109544, 01 2020. URL <https://doi.org/10.1016/j.jbiomech.2019.109544>.
- Alejandro Lopez-Perez, Rafael Sebastian, M Izquierdo, Ricardo Ruiz, Martin Bishop, and Jose M Ferrero. Personalized cardiac computational models: From clinical data to simulation of infarct-related ventricular tachycardia. *Front Physiol*, 10:580, 2019. URL <https://doi.org/10.3389/fphys.2019.00580>.
- Luigi Lovato, Mariano Cefarelli, Luca Di Marco, Daniel Arcioni, Giada Tortora, Ada Dormi, Nicolò Schicchi, Elisabetta Mariucci, Marco Di Eusanio, Davide Pacini, and Rossella Fattori. Marfan and loeys-dietz aortic phenotype: a potential tool for diagnosis and management. *JTCVS Open*, 2024. ISSN 2666-2736. doi: 10.1016/j.xjon.2024.03.015. URL <https://doi.org/10.1016/j.xjon.2024.03.015>.
- Pau Medrano-Gracia, John Ormiston, Mark Webster, Susann Beier, Alistair Young, Chris Ellis, Chunliang Wang, Örjan Smedby, and Brett Cowan. A computational atlas of normal coronary artery anatomy. *EuroIntervention : journal of EuroPCR in collaboration with the Working Group on Interventional Cardiology of the European Society of Cardiology*, 12(7):845–854, September 2016. ISSN 1774-024X. URL <https://doi.org/10.4244/eijv12i7a139>.
- Felix Meister, Helene Houle, Cosmin Nita, Andrei Puiu, Lucian Mihai Itu, and Saikiran Rapaka. 6 - additional clinical applications. In Tommaso Mansi, Tiziano Passerini, and Dorin Comaniciu, editors, *Artificial Intelligence for Computational Modeling of the Heart*, pages 183–210. Academic Press, 2020. ISBN 978-0-12-817594-1. URL <https://doi.org/10.1016/B978-0-12-817594-1.00017-6>.
- S. A. Niederer, Y. Aboelkassem, C. D. Cantwell, C. Corrado, S. Coveney, E. M. Cherry, T. Delhaas, F. H. Fenton, A. V. Panfilov, P. Pathmanathan, G. Plank, M. Riabiz, C. H. Roney, R. W. dos Santos, and L. Wang. Creation and application of virtual patient cohorts of heart models. *Philosophical Transactions of the Royal Society A: Mathematical, Physical and Engineering Sciences*, 378(2173):20190558, 2020. URL <https://dx.doi.org/10.1098/rsta.2019.0558>.
- OpenFOAM Foundation. OpenFOAM. URL <http://www.openfoam.org>. Last accessed: 2023-11-01.
- Phalla Ou, David S. Celermajer, Elie Mousseaux, Alain Giron, Yacine Aggoun, Isabelle Szezepanski, Daniel Sidi, and Damien Bonnet. Vascular remodeling after “successful” repair of coarctation: Impact of aortic arch geometry. *Journal of the American College of Cardiology*, 49(8):883 – 890, 2007. ISSN 0735-1097. URL <https://doi.org/10.1016/j.jacc.2006.10.057>.
- Romana Perinajová, Joe F. Juffermans, Jos J.M. Westenberg, Roel L.F. van der Palen, Pieter J. van den Boogaard, Hildo J. Lamb, and Saša Kenjereš. Geometrically induced wall shear stress variability in cfd-mri coupled simulations of blood flow in the thoracic aortas. *Computers in Biology and Medicine*, 133:104385, 2021. ISSN 0010-4825. URL <https://doi.org/10.1016/j.combiomed.2021.104385>.
- M. Piccinelli, A. Veneziani, D. A. Steinman, A. Remuzzi, and L. Antiga. A framework for geometric analysis of vascular structures: Application to cerebral aneurysms. *IEEE Transactions on Medical Imaging*, 28(8):1141–1155, 2009. URL <https://doi.org/10.1109/TMI.2009.2021652>.
- Les Piegl and Wayne Tiller. *The NURBS Book*. Springer-Verlag, New York, NY, USA, second edition, 1996.
- Bruno V. Rego, Dar Weiss, Matthew R. Bersi, and Jay D. Humphrey. Uncertainty quantification in subject-specific estimation of local vessel mechanical properties. *International Journal for Numerical Methods in Biomedical Engineering*, 37(12):e3535, 2021. URL <https://doi.org/10.1002/cnm.3535>.
- Cristobal Rodero, Marina Strocchi, Maciej Marciniak, Stefano Longobardi, John Whitaker, Mark D. O’Neill, Karli Gillette, Christoph Augustin, Gernot Plank, Edward J. Vigmond, Pablo Lamata, and Steven A. Niederer. Linking statistical shape models and simulated function in the healthy adult human heart. *PLOS Computational Biology*, 17(4):1–28, 04 2021. URL <https://doi.org/10.1371/journal.pcbi.1008851>.
- Pau Romero, Miguel Lozano, Francisco Martínez-Gil, Dolors Serra, Rafael Sebastián, Pablo Lamata, and Ignacio García-Fernández. Clinically-driven virtual patient cohorts generation: An application to aorta. *Frontiers in Physiology*, 12, 2021. ISSN 1664-042X. URL <https://dx.doi.org/10.3389/fphys.2021.713118>.
- Pau Romero, Giada S. Romitti, Ignacio García-Fernández, and Miguel Lozano. A fast and robust method for centerline approximation of vessel trees. In *International Conference on Computational and Mathematical Biomedical Engineering*, pages 64–67, 2022. URL <https://www.combiomed.net/2024/cmbe-proceedings.htm>.
- Caroline H. Roney, Ali Pashaei, Marianna Meo, Rémi Dubois, Patrick M. Boyle, Natalia A. Trayanova, Hubert Cochet, Steven A. Niederer, and Edward J. Vigmond. Universal atrial coordinates applied to visualisation, registration and construction of patient specific meshes. *Medical Image Analysis*, 55:65–75, 2019. ISSN 1361-8415. URL <https://doi.org/10.1016/j.media.2019.04.004>.
- M. Yousuf Salmasi, Selene Pirola, Sumesh Sasidharan, Serena M. Fisichella, Alberto Redaelli, Omar A. Jarral, Declan P. O’Regan, Aung Ye Oo, James E. Moore, Xiao Yun Xu, and Thanos Athanasiou. High wall shear stress can predict wall degradation in ascending aortic aneurysms: An integrated biomechanics study. *Frontiers in Bioengineering and Biotechnology*, 9, 2021. ISSN 2296-4185. URL <https://dx.doi.org/10.3389/fbioe.2021.750656>.

- Steffen Schuler, Nicolas Pilia, Danila Potyagaylo, and Axel Loewe. Cobiveco: Consistent biventricular coordinates for precise and intuitive description of position in the heart – with matlab implementation. *Medical Image Analysis*, 74: 102247, 2021. ISSN 1361-8415. URL <https://doi.org/10.1016/j.media.2021.102247>.
- Froso Sophocleous, Benedetta Biffi, Elena Giulia Milano, Jan Bruse, Massimo Caputo, Cha Rajakaruna, Silvia Schievano, Costanza Emanuelli, Chiara Bucciarelli-Ducci, and Giovanni Biglino. Aortic morphological variability in patients with bicuspid aortic valve and aortic coarctation. *European Journal of Cardio-Thoracic Surgery*, 55(4):704–713, 10 2018. ISSN 1010-7940. URL <https://doi.org/10.1093/ejcts/ezy339>.
- B Thamsen, P Yevtushenko, L Gundelwein, A A A Setio, H Lamecker, M Kelm, M Schafstedde, T Heimann, T Kuehne, and L Goubergrits. Synthetic database of aortic morphometry and hemodynamics: Overcoming medical imaging data availability. *IEEE Trans Med Imaging*, 40(5): 1438–1449, May 2021. URL <https://dx.doi.org/10.1109/TMI.2021.3057496>.
- Benjamin Urick, Travis M. Sanders, Shaolie S. Hossain, Yongjie J. Zhang, and Thomas J. R. Hughes. Review of patient-specific vascular modeling: Template-based isogeometric framework and the case for CAD. *Archives of Computational Methods in Engineering*, 26(2):381–404, 2019. ISSN 1886-1784. URL [10.1007/s11831-017-9246-z](https://doi.org/10.1007/s11831-017-9246-z).
- Alec Vahanian, Friedhelm Beyersdorf, Fabien Praz, Milan Milojevic, Stephan Baldus, Johann Bauersachs, Davide Capodanno, Lenard Conradi, Michele De Bonis, Ruggero De Paulis, Victoria Delgado, Nick Freemantle, Martine Gilard, Kristina H Haugaa, Anders Jeppsson, Peter Jüni, Luc Pierard, Bernard D Prendergast, J Rafael Sádaba, Christophe Tribouilloy, Wojtek Wojakowski, ESC/EACTS Scientific Document Group, and ESC National Cardiac Societies. 2021 ESC/EACTS Guidelines for the management of valvular heart disease: Developed by the Task Force for the management of valvular heart disease of the European Society of Cardiology (ESC) and the European Association for Cardio-Thoracic Surgery (EACTS). *European Heart Journal*, 43(7):561–632, 08 2021. ISSN 0195-668X. URL <https://doi.org/10.1093/eurheartj/ehab395>.
- Jinlin Wu, Mohammad A. Zafar, Yupeng Li, Ayman Saeyeldin, Yan Huang, Rui Zhao, Juntao Qiu, Maryam Tanweer, Mohamed Abdelbaky, Anton Gryaznov, Joelle Buntin, Bulat A. Ziganshin, Sandip K. Mukherjee, John A. Rizzo, Cuntao Yu, and John A. Eleftheriades. Ascending aortic length and risk of aortic adverse events: The neglected dimension. *Journal of the American College of Cardiology*, 74(15):1883–1894, 2019. ISSN 0735-1097. doi: <https://doi.org/10.1016/j.jacc.2019.07.078>.
- Hui Xie, Weiyu Xu, Ya Xing Wang, and Xiaodong Wu. Deep learning network with differentiable dynamic programming for retina oct surface segmentation. *Biomed. Opt. Express*, 14(7):3190–3202, Jul 2023. URL <https://doi.org/10.1364/BOE.492670>.
- Yongjie Zhang, Yuri Bazilevs, Samrat Goswami, Chandrajit L. Bajaj, and Thomas J.R. Hughes. Patient-specific vascular nurbs modeling for isogeometric analysis of blood flow. *Computer Methods in Applied Mechanics and Engineering*, 196(29):2943–2959, 2007. ISSN 0045-7825. URL <https://doi.org/10.1016/j.cma.2007.02.009>.